PHYSICAL REVIEW D VOLUME 15, NUMBER 11 1 JUNE 1977

Single-pion production in π^+p interactions near 1 GeV

P. L. Jain, Z. Ahmad, and G. Pappas
High Energy Experimental Laboratory, Department of Physics, State University of New York at Buffalo, Amherst, New York 14214

(Received 5 April 1976; revised manuscript received 21 June 1976)

A detailed analysis of the reaction $\pi^+p \to \pi^+p\pi^0$ at three different intermediate energies is presented. The final state involves significant production of N^{*++}, N^{*+}, and ρ^+. The single-particle distributions for π^+ and π^0 are presented.

I. INTRODUCTION

A considerable amount of data has recently become available concerning neutral- and charged-pion production in hadronic collision. The lowest primary pion momentum at which the charged-pion inclusive distribution has been studied is 3.7 GeV/c. The studies of inclusive π^0 distribution are difficult due to the low γ-detection efficiency of hydrogen-filled bubble chambers and the difficulties in covering a large solid angle with counter detectors. We present here the single charged-(π^+) and neutral-pion production distributions in reactions

$$\pi^+p \to \pi^+p\pi^0 \qquad (1)$$

$$\to \pi^+\pi^+n \qquad (2)$$

at four intermediate momenta, i.e., (i) 1.04, (ii) 1.22, (iii) 1.39, and (iv) 1.76 GeV/c. For more-than-one-particle distributions we present the following: (i) Dalitz plot, (ii) scatter plot, (iii) angular distribution, (iv) Peyrou plot, and (v) longitudinal-phase-space plot for the reaction (1) at three intermediate momenta of (i) 1.04, (ii) 1.22, and (iii) 1.39 GeV/c.

II. EXPERIMENTAL PROCEDURE

The data reported in this paper were obtained from an exposure at the BNL 20-in. hydrogen bubble chamber. A total of 9160 frames were taken at 1.04 GeV/c, 85 150 at 1.22 GeV/c, 7940 at 1.39 GeV/c, and 2938 at 1.76 GeV/c by using an electrostatically separated π^+ beam at the Cosmotron. The films for 1.22 and 1.76 GeV/c were scanned twice for events with two-prong topology in our laboratory. Events were measured on a machine called NRI. An IBM keypunch machine is connected to the NRI measuring machine so as to facilitate the transfer of data from the control panel and the x-y coordinates of the stage directly to the computer cards. The measurements were analyzed by using the geometrical-reconstruction program called TVGP and kinematic-fitting program called SQUAW, while the data at 1.04 and 1.39 were processed at Yale[1], through the reconstruction and kinematic-analysis programs called YACK and GUTS, respectively. Ionization information was estimated visually and was used in classifying the events. Thus, both kinematic fitting and estimates of bubble density were used for all events in order to determine particle and reaction identification. The analysis includes two or more visible prongs in π^++p interactions. The inelastic interaction for two visible prongs gives the abundant final products (i) $\pi^+p\pi^0$ and (ii) $\pi^+\pi^+n$. We present here the analysis of about 3400 events of type (i) and about 1100 events of type (ii) at four different energies. We may point out that reaction (i) involves a significant production of $N^{*++}(\pi^+p)$, $N^{*+}(\pi^0p)$, and $\rho^+(\pi^+\pi^0)$ and these channels account for about 95% of the entire π^0 production near 1 GeV. The one-constraint events were selected on the basis of the missing-mass-squared distribution with a cut of 2.5 standard deviations and on the basis of the goodness of the fit. The events with $\chi^2 \leq 6$ with a confidence level of 1% were used for one-constraint fit events. Thus the events with one π^0 were separated from those with one neutron by looking at the values for their missing masses and the χ^2 distributions. Some events which on the bases of missing-mass distribution alone were satisfied by two different hypotheses within the same class of constraints were finally resolved by accepting the hypothesis that yielded the smallest value of χ^2. In Figs. 1(A) and 1(B) are shown the distributions of the square of the missing mass for π^0 and n, respectively, for four primary beams (a), (b), (c), and (d). We observe a strong peak near the mass squared ~0.0183 and 0.883 GeV^2, i.e., for π^0 and neutron, respectively.

III. RESULTS AND DISCUSSION

Figures 2(a), 2(b), and 2(c) show a Dalitz plot for the $\pi^+p\pi^0$ final state. Formation of N^{*++}, N^{*+}, and ρ^+ is quite clear and N^{*++} is much more in abundance than N^{*+}. The clustering of the points at these resonances increases with the increase

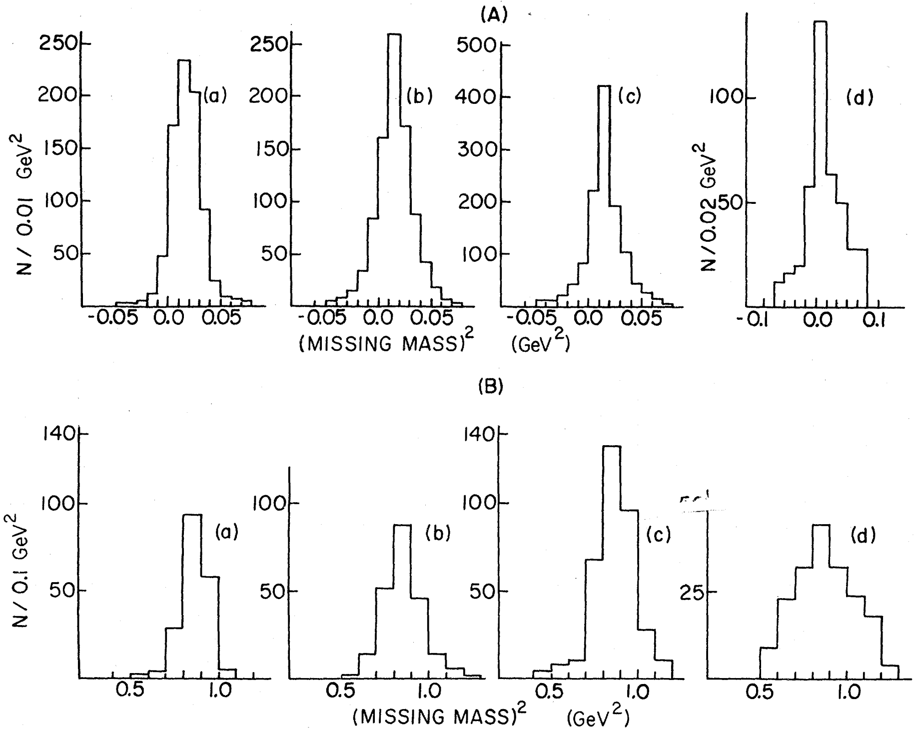

FIG. 1. Missing-mass distributions (A) for π^0 and (B) for n at (a) 1.04, (b) 1.22, (c) 1.39, and (d) 1.76 GeV/c.

in energy. In order to understand the nature of the exchanged particle involved in these resonances, we show in Figs. 3, 4, and 5 the scatter plots for invariant masses $M(\pi^+p)$, $M(\pi^0p)$, and $M(\pi^+\pi^0)$ vs four-momentum transfer squared $|t_{\pi^+\pi^0}|$, $|t_{\pi^+\pi^+}|$, and $|t_{\pi^+p}|$, respectively, for three primary beams. Figure 3 shows that there are two clusters in the N^{*++} resonance band. The strong concentration of particles at small-$|t_{\pi^+\pi^0}|$ values is very dominant at all the three energies, whereas the small cluster at large-$|t_{\pi^+\pi^0}|$ value is less dominant at 1.04 GeV/c but becomes strong at 1.39 GeV/c. The intense concentration of particles at small-t value in the N^{*++} band implies that most of the N^{*++} events are produced peripherally (i.e., with large impact parameter) and that the reaction proceeds mostly via meson exchange [Fig. 27(a)]. In Fig. 4, the concentration of events in the N^{*+} band is due to the exchange process [Fig. 27(e)]. In Fig. 5, there is a concentration of events for $M(\pi^+\pi^0) \geq 0.6$ GeV/c which is due to the reflection of the dominant N^{*++} resonance. We may also point out that a small concentration of events for $M(\pi^+p) > 1.4$ GeV in Fig. 4

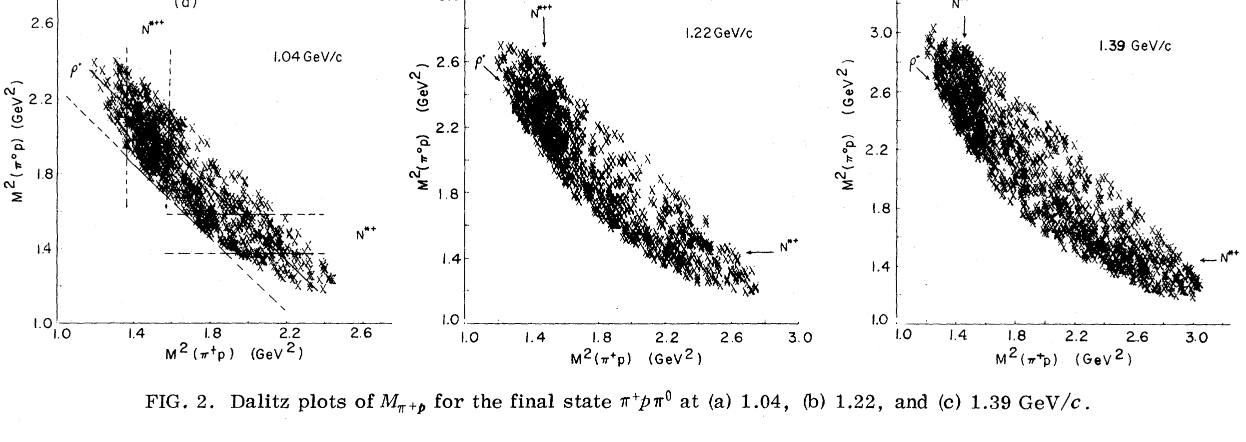

FIG. 2. Dalitz plots of M_{π^+p} for the final state $\pi^+p\pi^0$ at (a) 1.04, (b) 1.22, and (c) 1.39 GeV/c.

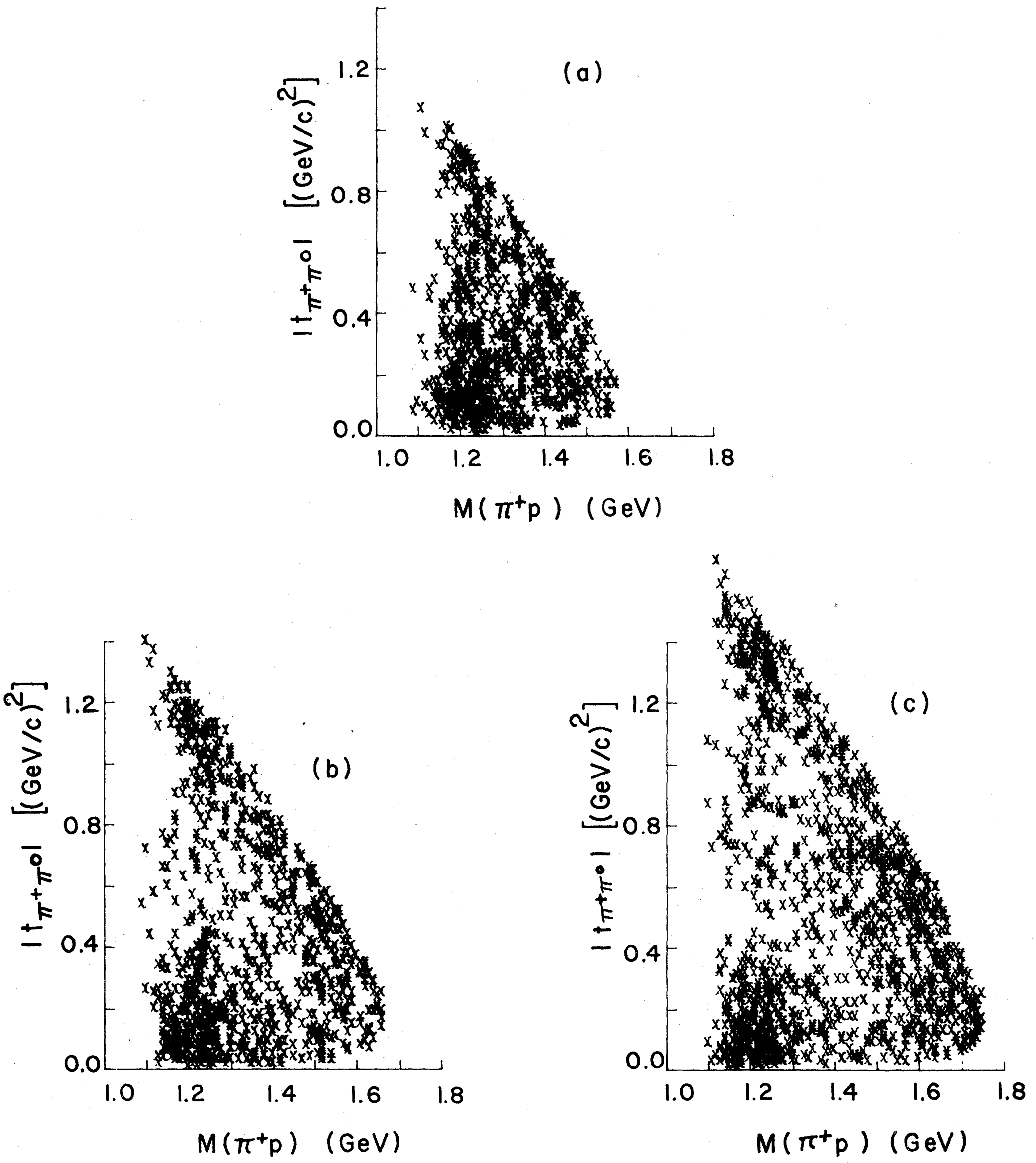

FIG. 3. Scatter plots of M_{π^+p} vs $|t_{\pi^+\pi^0}|$, for three beams (a) 1.04, (b) 1.22, and (c) 1.39 GeV/c, respectively.

are largely due to the reflection of the resonances N^{*+} and N^{*++}, respectively.

The single-particle c.m. angular distributions for $\pi^+p \rightarrow \pi^+p\pi^0$ as a function of the three beam energies are exhibited in Figs. 6 (π^+), 7 (p), and 8 (π^0), respectively. In each case the angle referred to is measured between the incoming beam pion and the denoted outgoing particle. One does not require the correction for this reaction as we are not dealing here with the absolute value of the cross section. The most prominent feature of the data is the rather flat distribution for π^+ and π^0 at 1.04 GeV/c and slow buildup of the forward peak as the energy of the projectile increases from 1.04 to 1.39 GeV/c. Since the forward and backward peaks in the angular distributions of the produced particles in the quasi-two-body reactions are generally due to the peripherally-produced resonances, the absence of the forward peak in Fig. 6 implies that the cross section for the peripherally produced resonance ρ^+ at this energy is very small. From the Dalitz plot (Fig. 2) we find that ρ^+ is produced in small amounts, and the scatter plot [Fig. 5(a)] also shows that, indeed, the cross section of peripherally produced ρ^+ is practically negligible. The relative buildup of the forward peak in Fig. 6(b) and 6(c) could be attributed to an increase in the peripherally produced ρ^+.

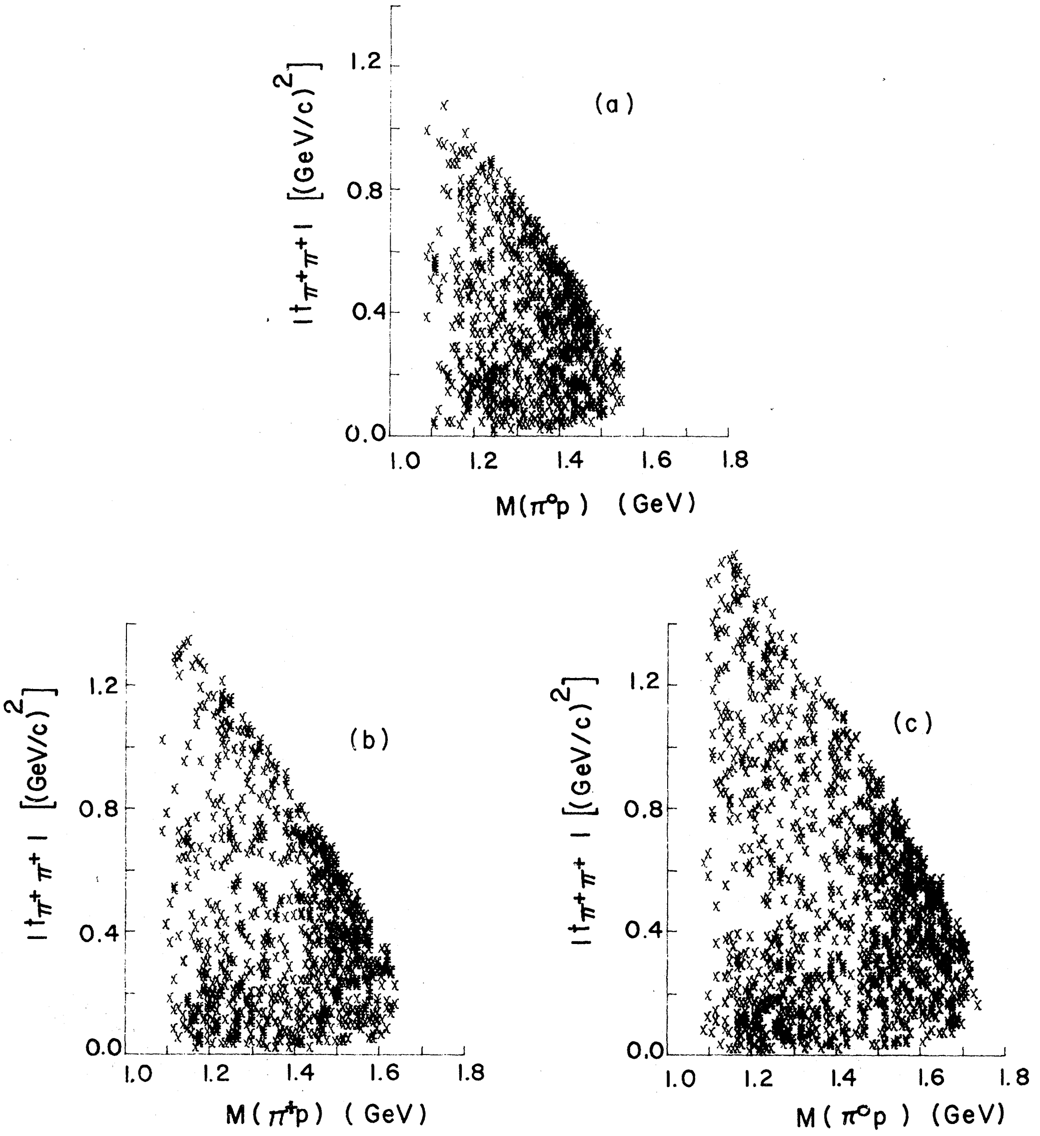

FIG. 4. Scatter plots of $M_{\pi^0 p}$ vs $|t_{\pi^+\pi^+}|$, for three beams (a) 1.04, (b) 1.22, and (c) 1.39 GeV/c, respectively.

This is supported by the scatter plots Figs. 5(b) and 5(c). The proton angular distributions in Figs. 7(a), 7(b), and 7(c) show a marked increase in peripheralism N^{*++} production with the increase in the primary energy. This is also indicated from the Dalitz plots as well as from scatter plots in Figs. 2–5. The backward and forward peaks in π^0 are also explained from Dalitz and scatter plots.

The forward-backward asymmetry given by the relation

$$A=(F-B)/(F+B)$$

is shown in Table I for each outgoing particle (π^+, p, π^0), where F and B are the numbers of forward ($\cos\theta>0$) and backward ($\cos\theta<0$) events, respectively, in the c.m. system for the three beams. In this table the polar-equatorial ratio $R=(P-E)/(P+E)$ is also shown for the three beams, where P and E are defined as the number of events with $|\cos\theta|>0.5$ and $|\cos\theta|<0.5$, respectively.

The longitudinal as well as the transverse momentum distributions of the final-state particles are studied through Peyrou plots, which are shown in Figs. 9, 10, and 11 for π^+, p, and π^0, respectively at the three beam energies. The $\langle p_t\rangle$ value for all the produced particles is ~0.2 GeV/c, while peak value for p_l is −0.1 GeV/c for π^+, −0.3, GeV/c for p, and 0.0 and 0.3 GeV/c for π^0. Table II contains the average values of the transverse and longitudinal momenta (i.e., $\langle p_l\rangle$ and $\langle p_t\rangle$) and

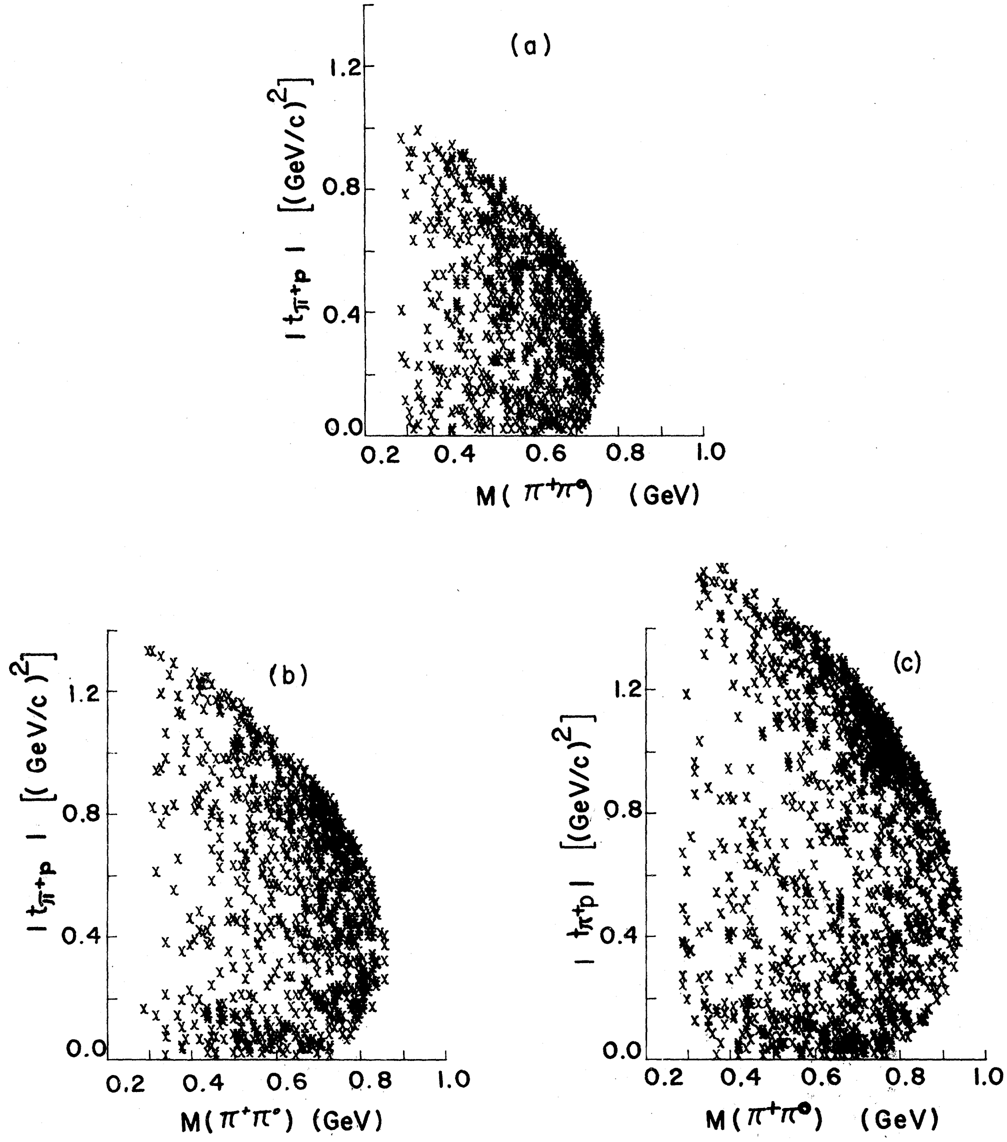

FIG. 5. Scatter plots of $M_{\pi^+\pi^0}$ vs $|t_{\pi^+p}|$, for three beams (a) 1.04, (b) 1.22, and (c) 1.39 GeV/c, respectively.

the average of the absolute values of the longitudinal momenta ($\langle|p_l|\rangle$) of π^+, p, and π^0 increase slowly with beam energies. We find that $\langle p_t\rangle$ and $\langle|p_l|\rangle$ for π^+, p, and π^0 increase slowly with beam energies, whereas $\langle p_l\rangle$ for the three particles is nearly zero.

The overall behavior exhibited in the distributions in the previous figures are summarized in the longitudinal-phase-space (LPS) plots[2] displayed in Figs. 12, 13, and 14 for the three different beams. The three axes, i.e., xx, yy, and zz, are inclined at angles of 120° with one another and correspond to $p_l(p)=0$, $p_l(\pi^+)=0$, and $p_l(\pi^0)=0$, respectively. The proton longitudinal momentum increases along BB' whereas the π^+ and π^0 longitudinal momentum increases along AA' and CC', respectively. For each event the c.m. longitudinal momenta measured perpendicularly from the signed diagonal lines for p, π^+, and π^0 intersect at a single point on the plot. In all the three plots, we find that due to the large "transverse mass" of the protons the distribution along $p_l(p)=0$ axis is rounded off more than any of the other two axes. In Fig. 12 we find that the LPS plot at 1.04 GeV/c is almost uniformly populated in the center with some noticeable concentration in the region marked as A. Clustering of particles in the region A goes on increasing with energy and also new concentra-

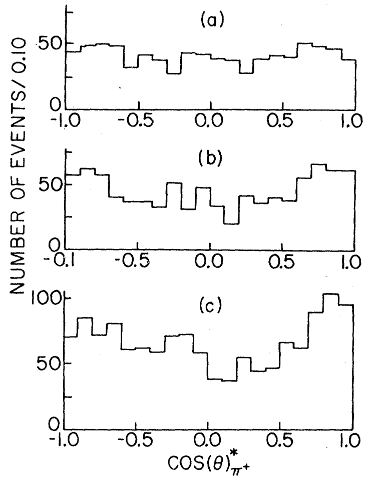

FIG. 6. The c.m. angular distribution of π^+, for three beams (a) 1.04, (b) 1.22, and (c) 1.39 GeV/c, respectively.

tion regions like B and C appear at higher energies. Region A is due to the resonance N^{*++} on the LPS plot.

Single-particle distributions for π^+ and π^0

The lowest primary-pion momentum at which the charged-pion inclusive properties have been studied so far is 3.7 GeV/c. But there is very little information available pertaining to inclusive π^0 production. In particular, the reaction $\pi^+ + p \to \pi^0 + X +$ anything has not been studied lower than 5 GeV/c. Whatever has been studied,[3] it has been through the decay mode of $\pi^0 \to 2\gamma$, while here we study this reaction through the missing-mass technique as discussed in Sec. II. At this low energy the cross section for more than one π^0 production in reaction (1) is very small so we can treat the distribution of the reaction with single-π^0 events as the major reaction with π^0 events. Thus, we present here the systematic study of experimental results for $\pi^+ + p \to X +$ anything ($X = \pi^0, \pi^+$) with incident momenta of (a) 1.04 GeV/c, (b) 1.22 GeV/c, (c) 1.39 GeV/c, and (d) 1.76 GeV/c in the target (laboratory) frame, the projectile frame, and in the c.m. system.

Valuable information about inclusive reactions comes from the study of transverse momentum squared (p_t^2) and the rapidity (Y) distributions of the produced particles. In Figs. 15(a) and 15(b) are shown the p_t^2 distribution for π^+ and π^0 for all beams. We observe that there is a peak at low p_t^2 in π^+ as well as in π^0. We have fitted each of these distributions with an exponential function of the form $Ae^{-Bp_t^2}$ and the values of the slopes (B)

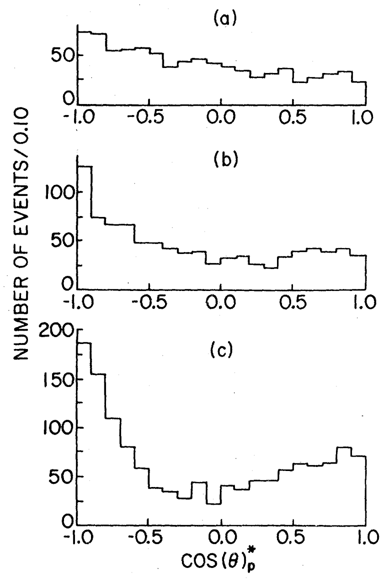

FIG. 7. The c.m. angular distribution of p for three beams (a) 1.04, (b) 1.22, and (c) 1.39 GeV/c, respectively.

are given in Fig. 15. The slopes for p_t^2 distribution decrease slowly with the increase in energy in both cases; however, $B(\pi^+)$ is a little higher than $B(\pi^0)$ at the same energy.

In inclusive reaction studies there is no empirical way to ascertain what kinematic and dynamical effects are involved in producing the sharp peaks in the distributions. Anthony *et al.*,[4] Biswas

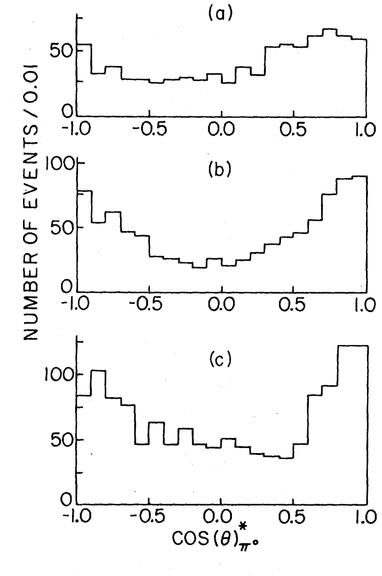

FIG. 8. The c.m. angular distribution of π^0 for three beams (a) 1.04, (b) 1.22, and (c) 1.39 GeV/c, respectively.

TABLE I. Asymmetry parameter $A=(F-B)/(F+B)$ and polar-equatorial ratio $R=(P-E)/(P+E)$ for π^+, p, and π^0.

	Beam (a) (1.04 GeV/c)	Beam (b) (1.22 GeV/c)	Beam (c) (1.39 GeV/c)
Asymmetry parameter			
$A(\pi^+)$	0.01 ± 0.06	-0.01 ± 0.05	0.04 ± 0.05
$A(p)$	0.27 ± 0.09	0.25 ± 0.09	0.14 ± 0.06
$A(\pi^0)$	-0.22 ± 0.03	-0.11 ± 0.04	-0.02 ± 0.04
Polar-equatorial ratio			
$R(\pi^+)$	0.08 ± 0.05	0.18 ± 0.05	0.18 ± 0.04
$R(p)$	0.08 ± 0.05	0.26 ± 0.05	0.40 ± 0.046
$R(\pi^0)$	0.17 ± 0.05	0.39 ± 0.055	0.29 ± 0.04

et al.,[5] and Ko and Lander[6] have shown that the value of the slope (B) varies significantly with the longitudinal momentum and depends strongly on the mass of the particle. Yen and Berger[7] have suggested that such peaks are caused primarily by peripheral production of low-mass resonance. We have already stated above that the resonance production of N^{*++}, N^{*+}, and ρ^+ is very dominant near 1 GeV. Such resonances are more important at low-multiplicity interactions and in the forward direction are expected to be predominantly of the same charge as the incident particle. The peaks should thus be smaller for forward produced π^0 than for π^+ from π^+p interactions. In Figs. 15(a) and 15(b) we find that the same energies the slopes for π^+ are larger than for π^0 in all four beams. Furthermore, we extracted the resonance $N^{*++}(\pi^+p)$ and $\rho^+(\pi^+\pi^0)$ from the reaction $\pi^+p\to\pi^+p\pi^0$ and $N^{*+}(\pi^+n)$ from the reaction $\pi^+p\to\pi^+\pi n$, by assuming that the effective mass of the resonance M_{res} lies between $(M_{\text{res}}+\Gamma)$ and $(M_{\text{res}}-\Gamma)$, where Γ is the full width of the resonance. We fitted each of these distributions with an exponential function of the form $Ae^{-Bp_t^2}$ and slope values B are given in Table III. We find that slope value B is practically the same for π^+ which are the decay products of the resonances $N^{*++}(\pi^+p)$ and $N^{*+}(\pi^+n)$ at all the three beam energies. Also the slope values π^+ and π^0 from resonance $\rho^+(\pi^+\pi^0)$ are equal at the same beam energy.

1. *Rapidity distribution*

The most interesting feature of meson-proton interactions which makes them different from proton-proton interactions is the asymmetry of the c.m. distribution of the produced pion. One of the possible ways of finding this asymmetry parameter is to look at rapidity distributions of the produced pions. Rapidity is defined as

$$Y=\tanh^{-1}(E/p_l)$$
$$=\tfrac{1}{2}\ln[(E+p_l)/(E-p_l)]\ .$$

The rapidity distributions have an approximately Gaussian shape for π^+ and π^0 and are shown in Figs. 16, 17, and 18 for π^+, π^0, and p, respectively, at three primary energies. The experimental data for π^+ and π^0 have practically the same distributions and are different from p-distributions.

We present the data in the target, center-of-

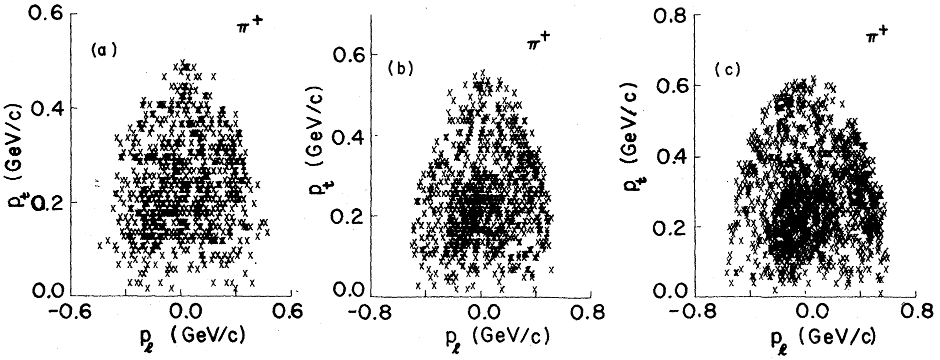

FIG. 9. Peyrou plots for π^+ for three beams (a) 1.04, (b) 1.22, and (c) 1.39 GeV/c, respectively.

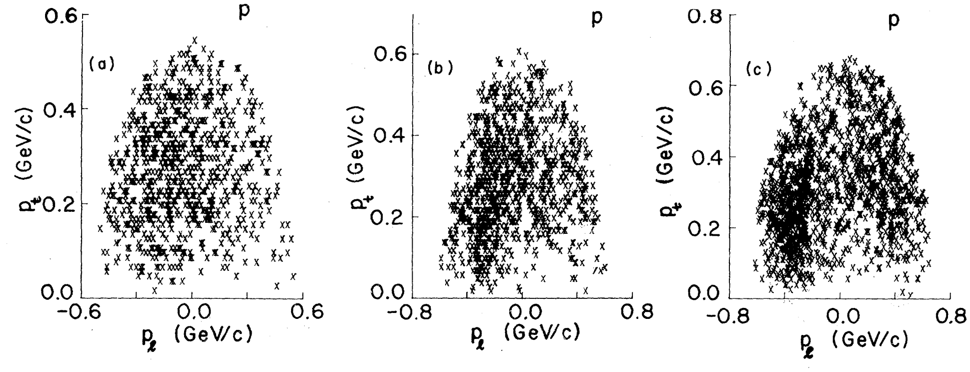

FIG. 10. Peyrou plots for p for three beams (a) 1.04, (b) 1.22, and (c) 1.39 GeV/c, respectively.

mass, and projectile frames and will investigate the energy dependence in target-fragmentation, pionization, and projectile-fragmentation regions. Also, by looking at the exclusive processes, we will explore which of the exclusive processes are contributing to the different kinematical regions of the inclusive spectra.

2. *Longitudinal-momentum distribution of π^+ in target, center-of-mass, and projectile frames*

In order to investigate the fragmentation of the target, we plot the structure function

$$G(p_l)=\int \frac{E_\pi}{\sigma_T}\,\frac{\partial^2\sigma}{\partial p_l \partial p_t{}^2 dp_t{}^2}\ ,$$

where all quantities are now evaluated in the laboratory system. Figure 19 shows the cross section $G(p_l\,(\mathrm{lab}))$ of π^+ at five different beam energies (i.e., at 1.04, 1.22, 1.39, 1.76, and 3.7 GeV/c) as a function of longitudinal momentum in the target frame. For the purpose of comparison, we have included the data of Alston-Garnjost *et al.*[8] at 3.7 GeV/c) wherever possible. However, the absolute normalization between the data of Alston-Garnjost *et al.* and the rest of the data should not be compared for two reasons. First, the Alston-Garnjost *et al.* data contain all multiplicities whereas the rest of the data are essentially from two-prong topology. Second, the Alston-Garnjost *et al.* data have been normalized by the asymtotic value of the cross section (24 mb) whereas the rest of the data have been normalized by the total cross section of the two exclusive channels ($\pi^+p \rightarrow \pi^+p\pi^0$ and $\pi^+p \rightarrow \pi^+\pi^+n$) in the two-prong topology. Since the two-prong cross section accounts for most of the total cross section at these energies we believe that the exclusions of large-multiplicity events have not affected the inclusive spectra in any significant way. The most striking feature of the data is the sharp increase in $G(p_l(\mathrm{lab}))<0.0$ GeV/c. In the hypothesis of limiting fragmentation, this region corresponds to the fragmentation of the target. However, it is a well-known fact that at these energies the quasi-two-body processes are very dominant. The larger contribution in this region arises from the formation and decay of N^{*++}, and an analysis of the pions from the resonances N^{*++} and N^{*+} show that these resonances contribute heavily towards the cross section in the fragmentation region.

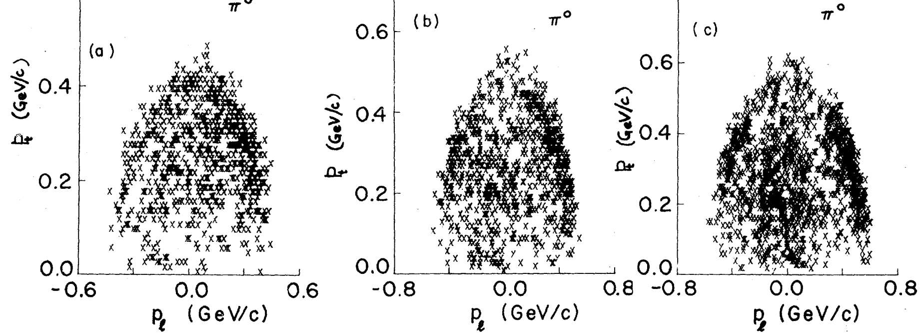

FIG. 11. Peyrou plots for π^0 for three beams (a) 1.04, (b) 1.22, and (c) 1.39 GeV/c, respectively.

TABLE II. The average values of transverse and longitudinal momentum of π^+, p, and π^0.

Particle	$\langle p_t\rangle$ (GeV/c)	$\langle p_l\rangle$ (GeV/c)	$\langle \lvert p_l\rvert\rangle$ (GeV/c)
		1.04 GeV/c	
π^+	0.228 ± 0.008	0.011 ± 0.004	0.155 ± 0.005
p	0.264 ± 0.009	-0.063 ± 0.002	0.187 ± 0.006
π^0	0.244 ± 0.008	0.056 ± 0.002	0.184 ± 0.006
		1.22 GeV/c	
π^+	0.240 ± 0.008	0.023 ± 0.001	0.191 ± 0.006
p	0.280 ± 0.009	-0.070 ± 0.002	0.234 ± 0.008
π^0	0.255 ± 0.008	0.047 ± 0.002	0.239 ± 0.008
		1.39 GeV/c	
π^+	0.270 ± 0.007	0.028 ± 0.001	0.215 ± 0.006
p	0.310 ± 0.008	0.058 ± 0.002	0.288 ± 0.008
π^0	0.275 ± 0.007	0.030 ± 0.001	0.247 ± 0.007

We define the invariant structure function

$$F(x)=\int [1/\sigma_T(E_\pi/\pi p_{\max})](\partial^2\sigma/\partial x\partial p_t^{\,2})dp_t^{\,2}$$

in the c.m. system as a function of x, where p_t is the transverse momentum of the pion, E_π is the energy of the pion in the c.m. system, and σ_T is the total cross section of the reaction. Figure 20 shows the π^+ spectra as a function of Feynman variable[9] x [$=p_l$ (c.m.)/$p_{\max}$(c.m.)]. We observe that the distributions are similar in shape at all the five energies. However, the cross section $F(x)$ increases very rapidly in the target-fragmentation region where the rate of increase in the cross section depends on the beam energy. For $-0.2<x<0.2$ the cross section is almost independent of momenta for the five beam energies. For

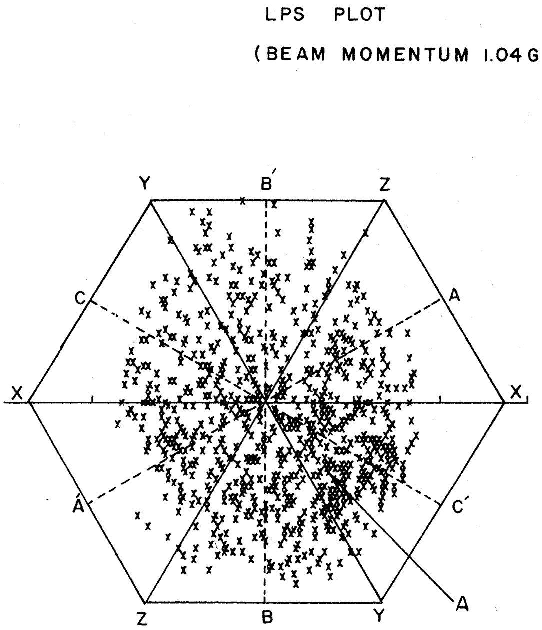

FIG. 12. Longitudinal-phase-space plot for 1.04 GeV/c.

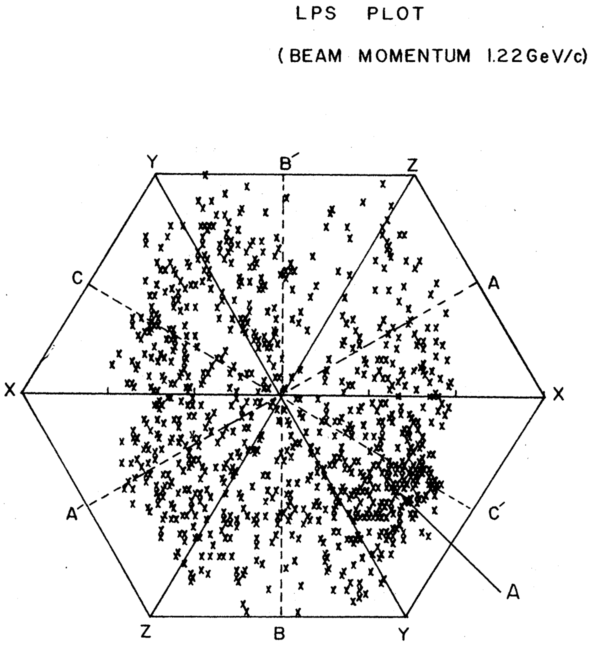

FIG. 13. Longitudinal-phase-space plot for 1.22 GeV/c.

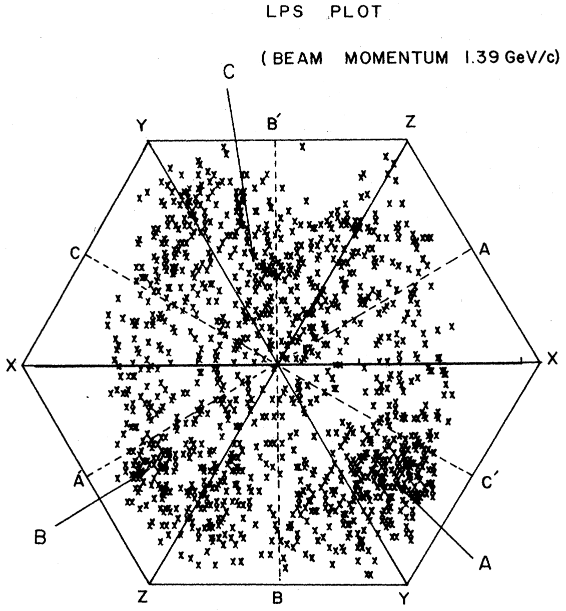

FIG. 14. Longitudinal-phase-space plot for 1.39 GeV/c.

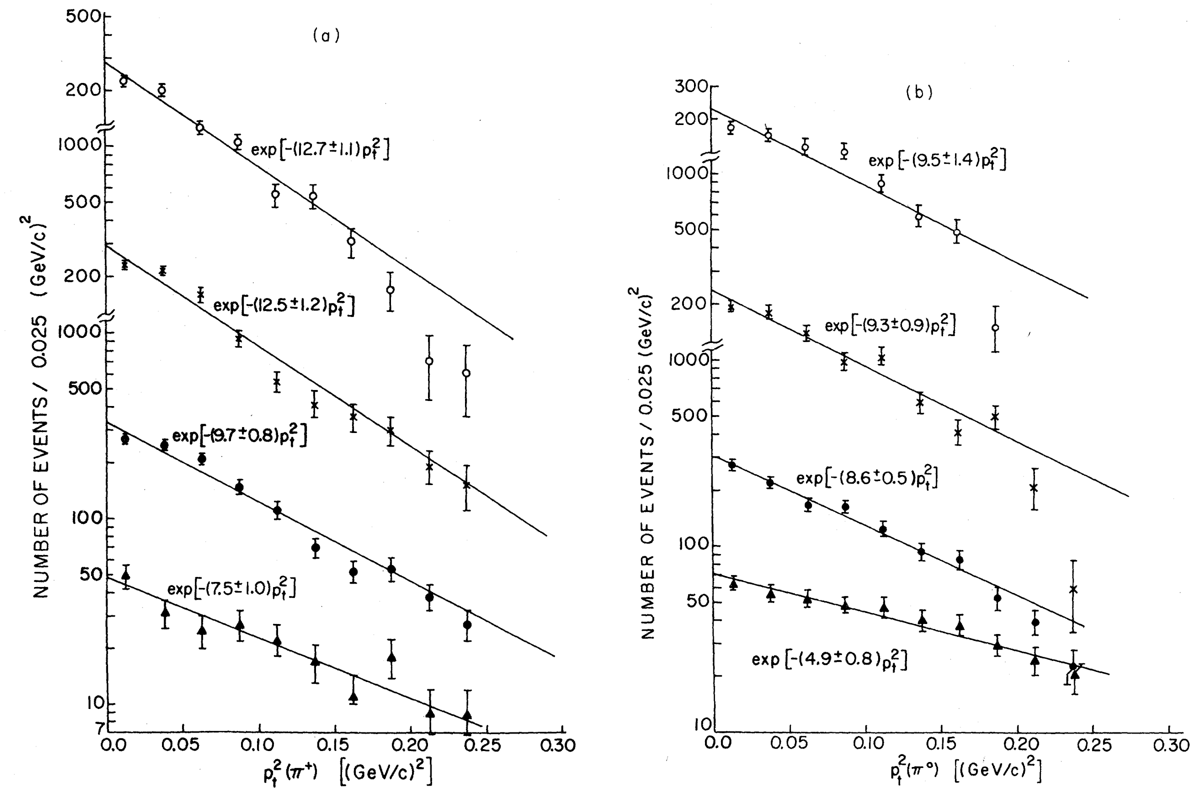

FIG. 15. The plot of dN/dp_t^2 (arbitrary scale) vs p_t^2 for (a) π^+ and (b) π^0 at 1.04 (○), 1.22 (×), 1.39 (●), and 1.76 GeV/c (△).

$0.2 < x < 0.5$ the cross sections at 1.04, 1.22, 1.39, and 1.76 GeV/c are close to one another and increase slowly with x.

In Fig. 21 we have presented the same data in the projectile rest frame. We find that the cross section at the four beam energies increases very rapidly for the region $0.0 \leq p_l(\text{proj}) \leq 0.8$ GeV/c and then varies slowly in the region $0.8 \leq p_l(\text{proj}) \leq 2.8$ GeV/c. This feature of the spectra in the projectile frame is similar to that seen in the target frame (Fig. 19). For $p_l(\text{proj}) \geq 2.8$ GeV/c we do not find any simple energy-dependent behavior.

3. Longitudinal-momentum distribution π^0 in target, center-of-mass, and projectile frames

Since the cross section for reactions resulting in two or more π^0 is extremely small at these energies, the π^0 spectra shown in Fig. 22 are essentially due to the exclusive reaction $\pi^+p \rightarrow \pi^+p\pi^0$. For $-0.3 < p_l(\text{lab}) < 0.2$ GeV/c the difference between various spectra is very apparent. Most of the π^0 near 1 GeV come from N^{*+} or ρ^+.

The π^0 spectra in the c.m. system are shown in Fig. 23 where the cross section has been expressed

TABLE III. The slope values B [in (GeV/c)$^{-2}$] of the exponential fit ($dn/dp_t^2 = Ae^{-Bp_t^2}$).

Beam momentum (GeV/c)	π^+ (all)	π^0 (all)	π^+ from $N^{*++}(\pi^+p)$	π^+ from $N^{*+}(\pi^+n)$	π^+ from $\rho^+(\pi^+\pi^0)$	π^0 from $\rho^+(\pi^+\pi^0)$
1.04	12.7±1.1	9.5±1.4	24.5±3.1	25.8±2.5	17.7±2.5	19.0±1.9
1.22	12.5±1.2	9.3±0.9	24.2±2.5	24.2±2.5	13.9±3.0	12.4±3.5
1.39	9.7±0.8	8.6±0.5	26.2±3.8	23.5±3.9	11.8±1.5	10.7±3.7
1.76	7.5±1.0	4.9±0.8	25.3±2.8	24.6±2.9	9.3±2.3	8.5±1.9

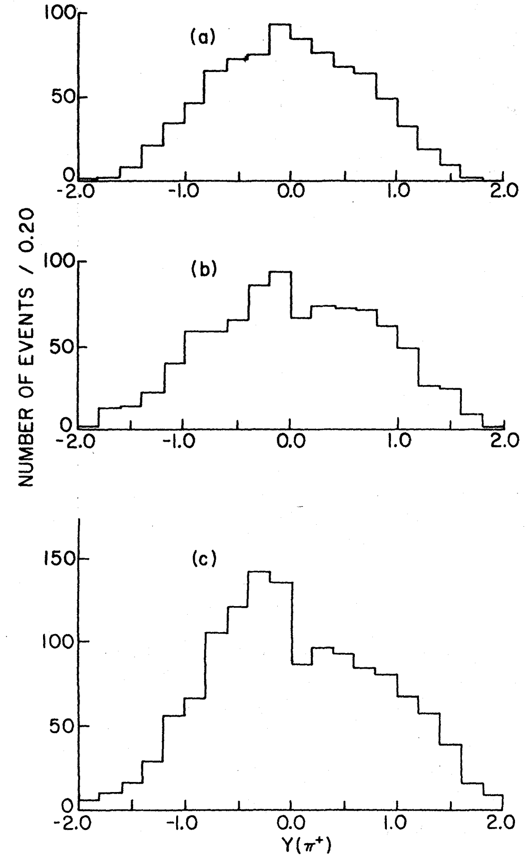

FIG. 16. Rapidity (Y) distribution for π^+ at (a) 1.04, (b) 1.22, and (c) 1.39 GeV/c, respectively.

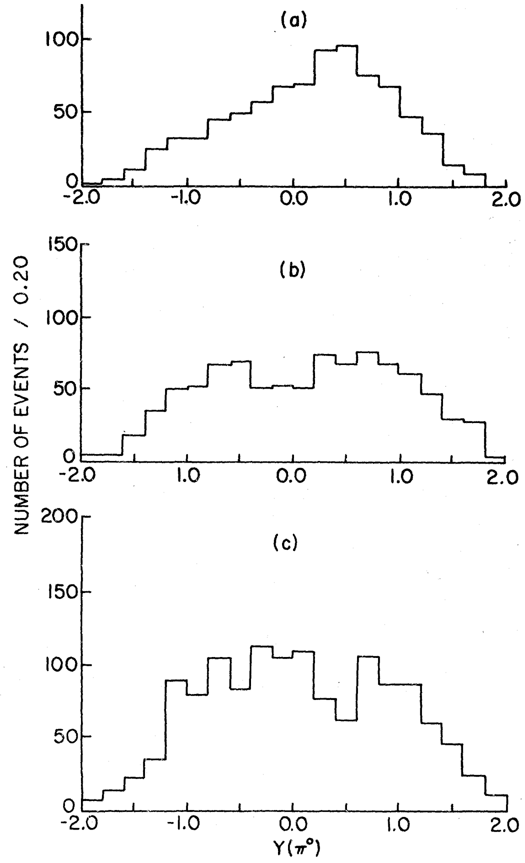

FIG. 17. Rapidity (Y) distribution for p at (a) 1.04, (b) 1.22, and (c) 1.39 GeV/c, respectively.

as a function of Feynman's variable x. For $x<-0.4$, which corresponds to the fragmentation region in the target frame, we find that the cross section decreases with an increase in the negative value of x at all four beam energies. Also, for $x<0.0$, the cross-section values at 1.22 and 1.39 GeV/c beam momenta are very close to one another. However, for $x>0$ we do not find any simple energy-dependent behavior.

In Fig. 24 we have presented the π^0 spectra in the projectile frame. The cross section shows a sharp increase for $0.0 \leq p_l(\text{proj}) \leq 0.4$ GeV/c at the four beam energies. For $p_l(\text{proj}) > 0.4$ GeV/c there is a marked fluctuation in the cross section and no simple energy-dependent behavior is evident. In the hypothesis of limited fragmentation, the region $0.0 < p_l(\text{proj}) < 0.4$ GeV/c belongs to beam fragmentation. Since below 2 GeV/c the π^+p scattering is predominantly a quasi-two-body reaction, a detailed analysis of resonance production show that N^{*++} produced via charge exchange contribute heavily in the beam-fragmentation region.

Recently, Biswas[10] suggested a scatter plot where the characteristics of an inclusive reaction can be visualized in all Lorentz frames translated along the direction of the beam. Figures 25 and 26 show the Biswas scatter plot of π^+ and π^0 produced in the reactions $\pi^+p \to \pi^+ +$ anything and $\pi^+ \to p\pi^0 +$ anything, respectively. In these plots each particle (i.e., π^+ or π^0) is represented by two variables, namely, $\mu p_l(p)$ and $Mp_l(t)$, where μ and M are the masses of the projectile and the target; and $p_l(p)$ and $p_l(t)$ are the longitudinal momenta of the π^+ (π^0) in the projectile and the target frames, respectively. An examination of Figs. 25(a)–25(c) indicates that most of the π's have their p_t^2 values restricted between 0.0 and 0.1 $(\text{GeV}/c)^2$, and there is a small cluster in Fig. 25(a) which is bounded by $0<x<-0.4$ and $0<p_t^2 \leq 0.1$ $(\text{GeV}/c)^2$. This cluster is also present in Figs. 25(b) and 25(c) and becomes more prominent with the beam energy. The region of the phase space where this

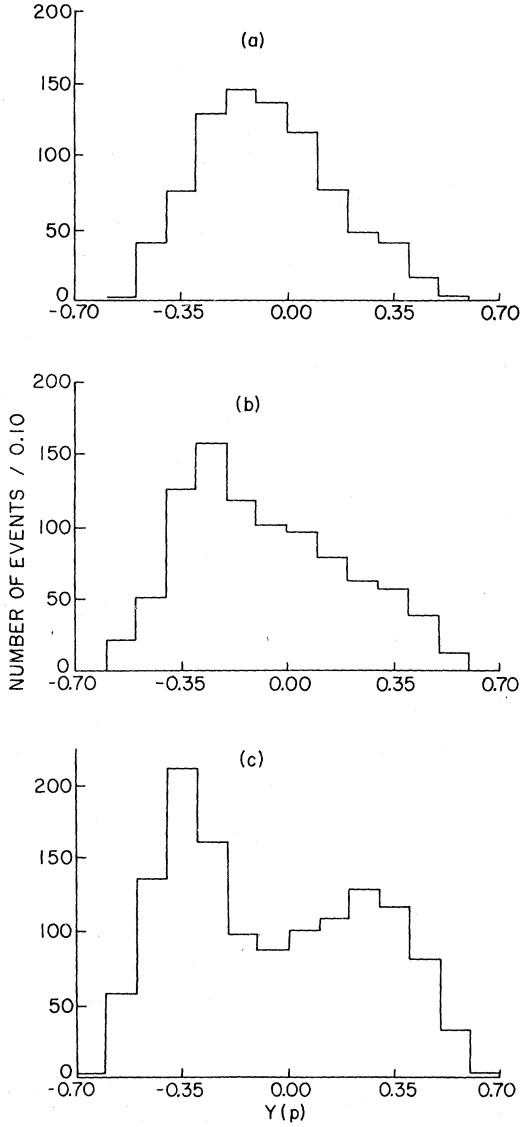

FIG. 18. Rapidity (*Y*) distribution for π^0 at (a) 1.04, (b) 1.22, and (c) 1.39 GeV/*c*, respectively.

cluster appears includes both the PR (pionization region) and the TFR (target-fragmentation region). The pions corresponding to this cluster possess small longitudinal momentum in the target frames.

To determine the possible origin of the cluster we have depicted in Figs. 27(a)–27(d) the resonance diagrams that will produce positive pions with small longitudinal momentum in the target frame. However, we know that in the exclusive channel $\pi^+p \to \pi^+p\pi^0$ the most dominant resonance is N^{*++}, and the exclusive channel $\pi^+p \to \pi^+\pi^+n$ proceeds mainly via the formation of the resonance N^{*+}. Hence we conclude that the major contribution to the above cluster comes from the resonances N^{*++} and N^{*+} produced via the diagram 27(a) and 27(b). The π^+ produced via the resonance diagrams 27(e) and 27(f) possess small longitudinal momentum in the projectile frame. In Fig. 25(b) we find a small cluster in the region $x > 0.4$ in the projectile-fragmentation region (PFR) which becomes very prominent in Fig. 25(c). Since the π^+ scatter plot also contains the pions from the reaction $\pi^+p \to \pi^+\pi^+n$, it is obvious that the diagrams 27(b) and 27(d) will also contribute to the cluster in the PFR. From the absence of

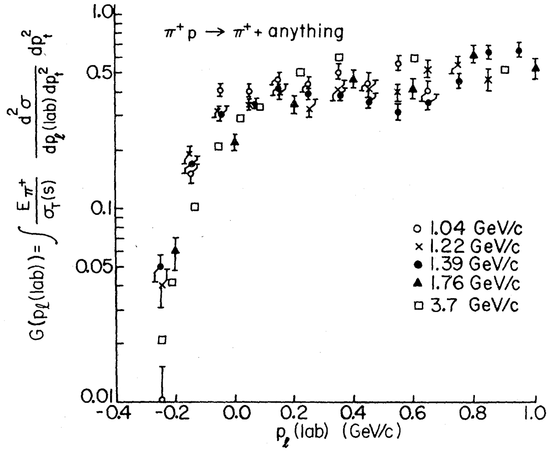

FIG. 19. The structure function $G(p_l\,(\text{lab}))$ in the target frame as a function of p_l (lab) for π^+ at 1.04, 1.22, 1.39, 1.76 and 3.7 GeV/*c*.

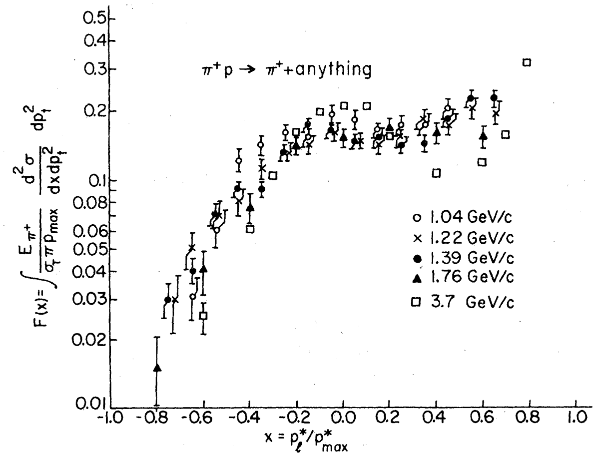

FIG. 20. The structure function *F* (*x*) as a function of *x* in the c.m. system for π^+ at 1.04, 1.22, 1.39, 1.76, and 3.76 GeV/*c*.

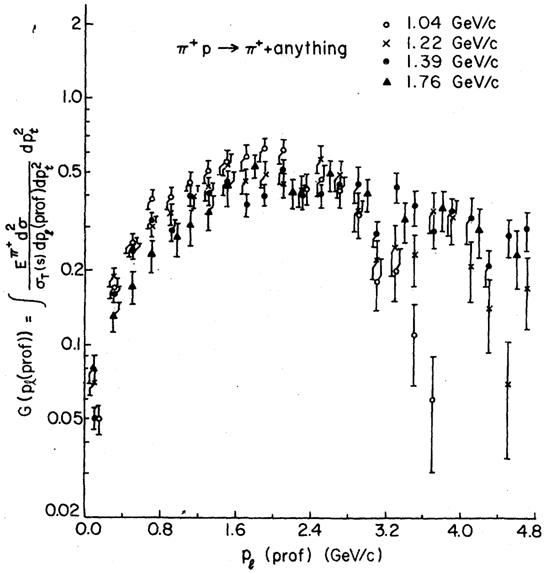

FIG. 21. $G(p_l(\text{proj}))$ vs $p_l(\text{proj})$ for π^+ at 1.04, 1.22, 1.39, and 1.76 GeV/c.

the forward peak in the angular distributions of the protons and neutrons in the center-of-mass frame we find that the contributions from baryon-exchange diagrams 27(d) and 27(g) to the cluster in the PFR and from the diagrams 27(c) and 27(f) to the cluster in the PR-TFR region are very small. Hence, we conclude that the cluster in the PFR is mostly due to the resonances $N^{*+}(\pi^0 p; \pi^+ n)$ and ρ^+ produced via the resonance diagrams 27(b), 27(e), and 27(f).

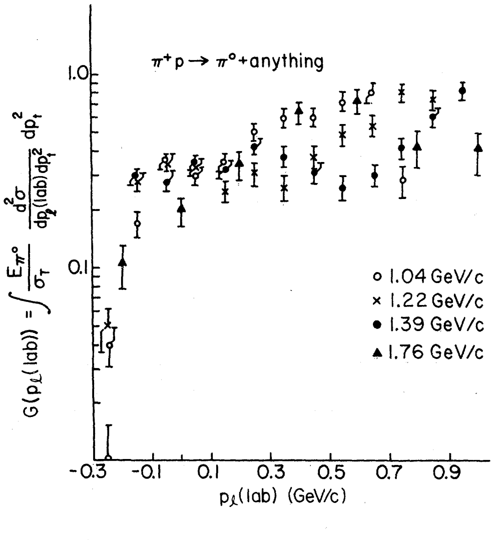

FIG. 22. $G(p_l(\text{lab}))$ vs $p_l(\text{lab})$ for π^0 at 1.04, 1.22, 1.39, and 1.76 GeV/c.

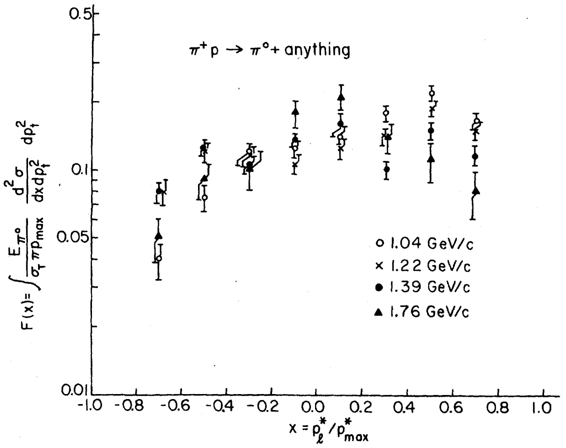

FIG. 23. $F(x)$ vs x in c.m. system for π^0 at 1.04, 1.22, 1.39, and 1.76 GeV/c.

The most important feature of the π^0 scatter plots [Figs. 26(a), 26(b), and 26(c)] is the large concentration of π^0 in the PFR. These π^0 have their longitudinal momenta restricted between 0.0 and 1.6 GeV/c in the projectile frame. However, their longitudinal momenta in the target frame is greater than 0.4 GeV/c in Fig. 26(a), 0.6 GeV/c in Fig. 26(b), and 0.7 GeV/c in Fig. 26(c). From the π^0 spectra in the projectile frame we find that these π^0 contributed heavily towards the cross section in

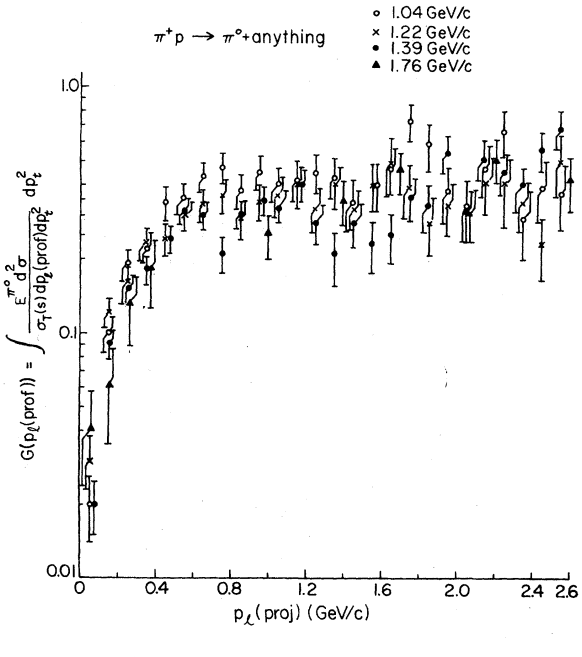

FIG. 24. $G(p_l(\text{proj}))$ vs $p_l(\text{proj})$ for π^0 at 1.04, 1.22, 1.39, and 1.76 GeV/c.

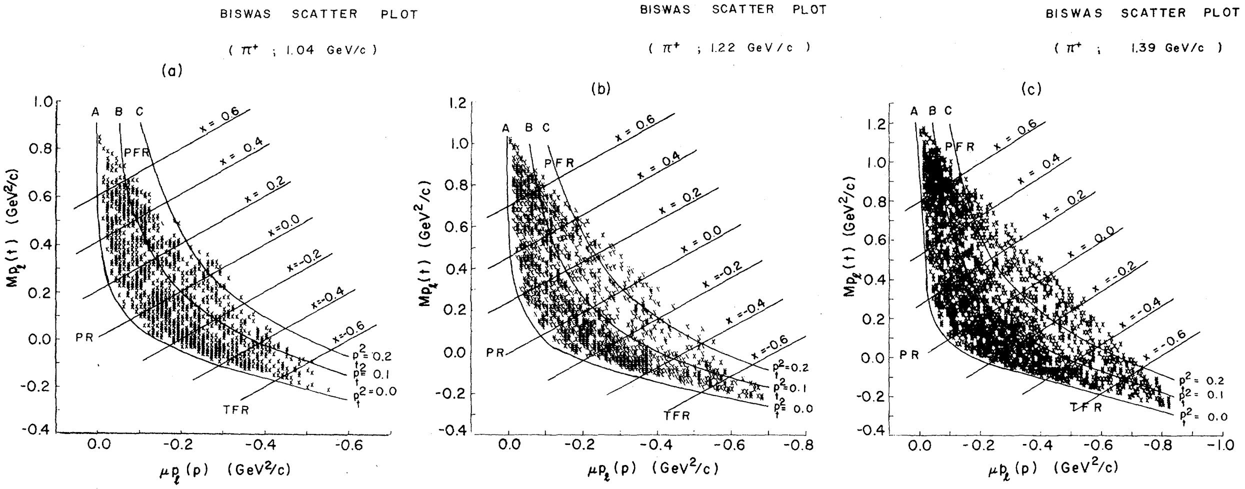

FIG. 25. Plot of longitudinal momentum of π^+ in the target rest frame as a function of its longitudinal momentum in the beam (projectile) rest frame for (a) 1.04, (b) 1.22, and (c) 1.39 GeV/c. The curves show this relation for different values of p_t^2 and x. PFR (projectile-fragmentation region), PR (pionization region) and TFR (target-fragmentation region).

the region $0.0 < p_l(\text{proj}) < 1.6$ GeV/c at all the three beam energies. Incidentally, in this region the cross section at the beam energies are very close to one another. The large concentration of π^0 in the PFR can be explained as due to the dominant contribution of the diagram 27(a). The contribution from the diagrams 27(e) and 27(f) enhance the concentration in the TFR and PFR, respectively, which increases with the beam energy.

IV. CONCLUSION

At intermediate energies, a reaction $\pi^+p \to \pi^+p\pi^0$ involves a significant production of resonances $N^{*++}(\pi^+p)$, $N^{*+}(\pi^0p)$, and $\rho^+(\pi^+\pi^0)$ and the peripheral-production mechanisms play a major role here. Our results on single-particle studies for π^+ and π^0 are the first attempt to analyze the reaction below 3.7 GeV/c. The Biswas plot provides

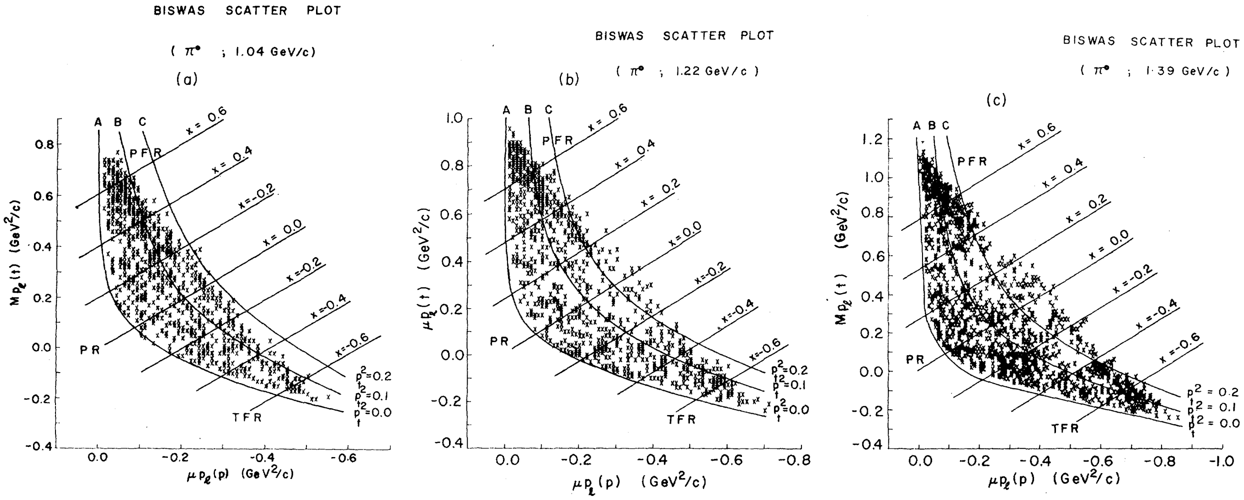

FIG. 26. Mp_l(target) vs μp_l(proj) for π^0 at (a) 1.04, (b) 1.22, and (c) 1.39 GeV/c for different values of p_t^2 and x.

an opportunity to visualize the entire inclusive-reaction data in all Lorentz frames translated along the beam direction. Our analysis of spectra as a function of longitudinal momentum in the target and the projectile frame show that the spectra at all the four beam energies are similar in shape in the target- as well as the projectile-fragmentation regions. They are similar (in shape) to the spectra for the same reaction obtained at higher energies. The π^0 spectra as a function of longitudinal momentum either in the target or in the projectile frame show similar behavior over a small interval of longitudinal momentum as for π^+. More data on the study of π^0 produced by π^+ and π^- beams at higher energies is highly desirable.

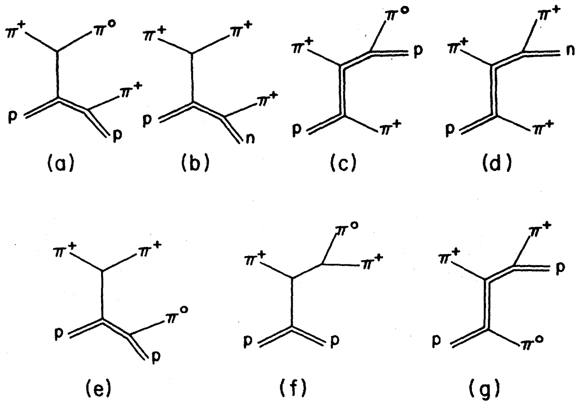

FIG. 27. Feynman diagrams for reactions $\pi^+p \rightarrow \pi^+p$ or $\pi^+\pi^+n$.

---

[1] We are very grateful to Professor H. L. Kraybill for generously providing us some data at 1.04 and 1.39 GeV/c. We are also very thankful to him for the use of films at two other energies.

[2] L. Van Hove, Nucl. Phys. B9, 331 (1969).

[3] G. Burleson *et al.*, Phys. Rev. D 12, 2557 (1975).

[4] R. W. Anthony *et al.*, Phys. Rev. Lett. 26, 38 (1971).

[5] N. N. Biswas *et al.*, Phys. Rev. Lett. 26, 1589 (1971).

[6] W. Ko and R. Lander, Phys. Rev. Lett. 26, 1064 (1971).

[7] E. Yen, and E. L. Berger, Phys. Rev. Lett. 24, 695 (1970).

[8] M. Alston-Garnjost, K. W. Barnham, M. S. Rabin, A. Barbaro-Galtieri, S. M. Flatté, J. H. Friedman, G. R. Lynch, J. N. MacNaughton, F. T. Solmitz, C. Risk, W. D. Shepard, J. T. Powers, N. N. Biswas, N. M. Cason, V. P. Kenny, and D. W. Thomas, Phys. Lett 39B, 402 (1972).

[9] R. P. Feynman, Phys. Rev. Lett. 23, 1415 (1969); J. Benecke, T. T. Chou, C. N. Yang, and E. Yen, Phys. Rev. 188, 2159 (1969).

[10] N. N. Biswas, Phys. Rev. D 6, 3127 (1972).